# Near-threshold propagation of mode II and mode III fatigue cracks in ferrite and austenite

T. Vojtek [a,b,*], R. Pippan [c], A. Hohenwarter [d], L. Holáň [a], J. Pokluda [a,b]

[a] Faculty of Mechanical Engineering, Brno University of Technology, Technická 2, CZ-61669 Brno, Czech Republic
[b] Central European Institute of Technology, Brno University of Technology, Technická 10, CZ-61600 Brno, Czech Republic
[c] Austrian Academy of Sciences, Erich Schmid Institute of Materials Science, Jahnstr. 12, A-8700 Leoben, Austria
[d] Department of Materials Physics, Montanuniversität Leoben, Jahnstr. 12, A-8700 Leoben, Austria

## Abstract

The near-threshold behavior of mode II and mode III long fatigue cracks in ferritic (ARMCO iron) and austenitic (X5CrNi18-10) steel were experimentally studied using various samples specially prepared to obtain the effective threshold values $\Delta K_{\mathrm{IIeff,th}}$ and $\Delta K_{\mathrm{IIIeff,th}}$. In both investigated materials, the effective thresholds for mode III were ∼1.7 times higher than those for mode II. Three-dimensional topological data obtained by the examination of fracture surfaces using stereophotogrammetry were utilized to identify crack growth micromechanisms. In austenite, mode I branching of both the mode II and mode III cracks started at the very onset of crack growth. On the other hand, all cracks in ferrite propagated in crystallographically assisted local mixed mode I + II + III with mode II dominance. These experimental results can be understood in terms of crack growth micromechanisms according to a deformation model in ferrite and a decohesion model in austenite. The dissimilarity of growth mechanisms in ferrite and austenite may be attributed to a different number of available slip systems in body-centered cubic and face-centered cubic metals.
© 2013 Acta Materialia Inc. Published by Elsevier Ltd. All rights reserved.

*Keywords:* Effective threshold; Shear-mode fatigue cracks; Ferrite; Austenite; Dislocation crack growth models

## 1. Introduction

Under small-scale yielding conditions the threshold of stress intensity range is an important mechanical property of a material that determines the conditions from non-propagation to propagation of a cyclically loaded crack. In order to discuss the crack propagation phenomena near the threshold stress intensity, it is helpful to divide the different mechanisms into two groups – extrinsic and intrinsic mechanisms – as proposed by Ritchie [1]. The intrinsic mechanisms are responsible for the generation of new fracture surfaces at the crack tip, i.e. the fatigue crack propaga-

tion. The most important extrinsic mechanisms occur in the surrounding of the crack tip as contacts of fracture surfaces during the cyclic loading, usually called crack closure. They reduce the real acting crack driving force at the crack tip, which, in the fatigue community, is called the effective driving force or the effective stress intensity range. Hence the resistance against the onset of fatigue crack growth, the threshold of stress intensity range, consists of an effective threshold and a contribution induced by crack closure.

For mode I loading, i.e. a cyclic loaded crack under tension, a vast number of papers have been devoted to the experimental analyses of both the effective threshold of stress intensity range and the effect of the fracture surface contact (see e.g. Refs. [1,2]). The situation for mode II and mode III loading, the in-plane and the out-of-plane cyclic shear loaded crack, respectively, is substantially different. The fracture surface contact, friction and fracture

* Corresponding author at: Faculty of Mechanical Engineering, Brno University of Technology, Technická 2, CZ-61669 Brno, Czech Republic. Tel.: +420 776711529.
*E-mail address:* tomas.vojtek@ceitec.vutbr.cz (T. Vojtek).

surface sliding have a more significant effect on the crack driving force than the mode I loading and it may have an impact on the crack propagation direction (e.g. Refs. [2–5]). The change in the crack growth direction is related to a competition between shear and opening loading modes that can lead to mode I branching. This phenomenon is mostly observed in the near-threshold region and Paris regime while in the high loading ranges, i.e. in the large scale yielding case, the cracks usually propagate co-planar along the maximum shear plane (e.g. Refs. [4,6–8]). Some simple concepts for the description of the mode I branching condition for mode II cracks were also proposed [9,10] but their verification is difficult due to a lack of reliable effective values of $\Delta K_{\mathrm{IIeff}}$. Thus the interaction between crack sliding and the deviation from the ideal mode II and mode III crack propagation induces inherent difficulties in the analyses of the mode II and mode III fatigue crack growth data. In order to avoid these difficulties there was an attempt to separate the problems of fracture surface sliding and the change of crack path by performing fatigue experiments under mode II and mode III loading conditions on samples with nearly ideal fatigue pre-cracks, i.e. exhibiting no initial crack flank interference.

The aim of the present experiments is to investigate the effective threshold under mode II and mode III loading and the crack path in the near threshold regime. These results will then be used to analyze the underlying mechanisms for the effective threshold for all types of loading modes, i.e. for modes I, II and III. The basic idea of the experiments is to start the mode II and mode III fatigue crack propagation with a nearly perfect pre-crack, which means no contact of the pre-crack flanks and a plane pre-crack with a sharp and straight crack front. In order to fulfill the requirement as well as possible, a fatigue pre-crack was generated under pure cyclic compression in different types of samples. Such cracks are open in the unloaded state, otherwise they would not propagate in compression. They are relatively planar and their crack front is fairly smooth. The samples are then recrystallized to avoid any effect of pre-fatigue, i.e. hardening of the material or the residual stresses. The applied technique is similar to the experiments performed to investigate the effective mode I threshold and to study the formation of crack closure during propagation of a crack subjected to mode I loading [11–13].

## 2. Materials and experimental arrangements

Two single-phase materials were investigated. The first material used was ARMCO iron (99.99% Fe), hereafter called ferrite, as a representative of a body-centered cubic (bcc) metal. The pre-material was cold-drawn. The chemical composition was as follows (wt.%): C 0.009, Mn 0.06, P 0.009, S 0.007 and Fe (balance). A cold rolled austenitic steel X5CrNi18-10 was selected as the second material as a representative of a face-centered cubic (fcc) metal. The chemical composition was as follows (wt.%): C 0.03, Si 1.00, Mn 2.00, Cr 17.00–19.50, Ni 8.50–11.50, N 0.12–0.22, Fe (balance).

Three experimental setups were used for modes II, III and II + III fatigue crack loading: simple shear (Fig. 1), compact tension shear (Fig. 2) and torsional. Before the beginning of all three types of experiments, pre-cracks were created at the notch root by compressive cyclic loading ($\Delta K_{\mathrm{I}} = 20$ MPa m$^{1/2}$, $R = 20$) in mode I. This loading helped to generate smooth fracture surfaces and produce detectable crack opening after compressive loading. It is well known that this kind of loading leads to open crack flanks, and this reduces the interaction of asperities in the crack wake, see Fig. 3.

After pre-fatigue loading, the specimens were annealed (heated up to 950 °C and cooled down slowly in vacuum), which eliminates the influence of a plastic zone and residual stresses at the crack front and causes a further smoothening of pre-crack facets. This resulted in a 0.2% offset yield strength, $\sigma_{\mathrm{y}}$, of ∼150 MPa and a mean grain size of ∼110 μm in ferrite and a yield strength, $\sigma_{\mathrm{y}}$, of ∼230 MPa and a grain size, $d_{\mathrm{m}}$, of ∼15 μm in austenite. In this way, the crack closure effects could be substantially suppressed at the beginning of the experiment and the measured threshold values could be considered to be very close to the effective values. After the shear-mode experiment, the ferritic specimens were fractured in liquid nitrogen and the austenitic specimens were subjected to cyclic loading in mode I until fracture. In the three experiments, the number of loading cycles for the propagation of a shear-mode crack of length $l_{\mathrm{s}}$ was usually $N = 10^5$ and the cyclic stress ratio was $R = 0.1$.

To load a single specimen simultaneously by remote simple shear in mode II, mode III and mixed mode II + III, a testing device has been designed and utilized. This device transformed tensile forces to the shear stress in circumferentially notched cylindrical bars with an inner diameter $d = 12$ mm and the outer diameter $D = 25$ mm (Fig. 1). At the exact central point of the bar the bending moment was zero when considering ideal testing conditions, and therefore no superposition of mode I was present. The circumferential crack was subjected to cyclic shear loading that resulted in various combinations of modes II and III as a function of the polar angle $\varphi$ (Fig. 1). At the top and the bottom of the circular cross-section the crack was loaded in a pure mode II, on the left and right in a pure mode III and, in between, a mixed-mode II + III loading was applied.

The pre-cracks started at the notch of depth $l_{\mathrm{n1}} = 6.5$ mm and reached length $l_{\mathrm{o}}$. The lengths $l_{\mathrm{o}}$ and $l_{\mathrm{s}}$ were measured in scanning electron microscopy (SEM) images of fracture surfaces. The dependences of mode II and mode III stress intensity factors (SIFs) on both the fatigue crack length $l_{\mathrm{o}} + l_{\mathrm{s}}/2$ and the angle $\varphi$ were calculated using field emission microscopy (FEM). Based on these results, dimensionless geometrical factors $Y_{\mathrm{II}}$, $Y_{\mathrm{III}}$ were evaluated (Eq. (1)) using a power regression function and plotted in Fig. 4.
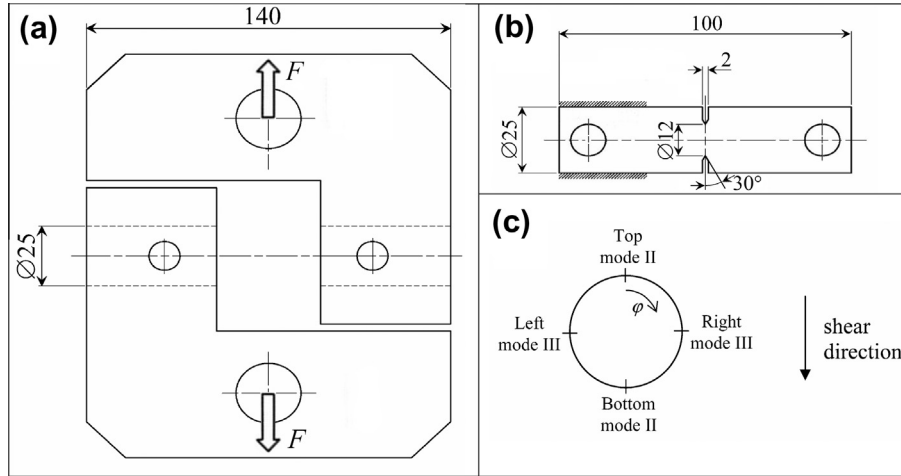
Fig. 1. Scheme of the experiment with cylindrical specimens loaded in pure shear: (a) loading device; (b) pure shear specimen; (c) specimen cross section with the corresponding loading modes.
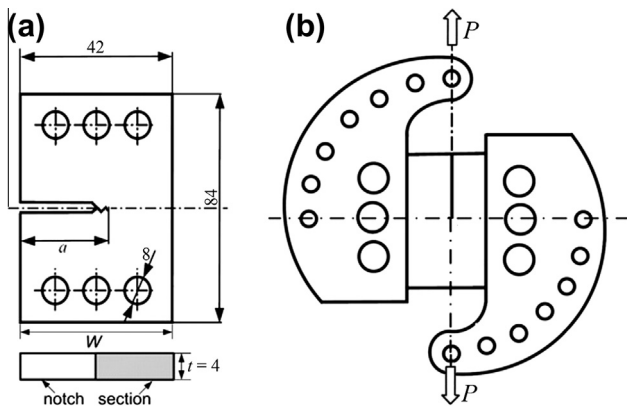


Fig. 2. Mode II experiment scheme: (a) compact tension shear (CTS) specimen; (b) scheme of the loading device [14].
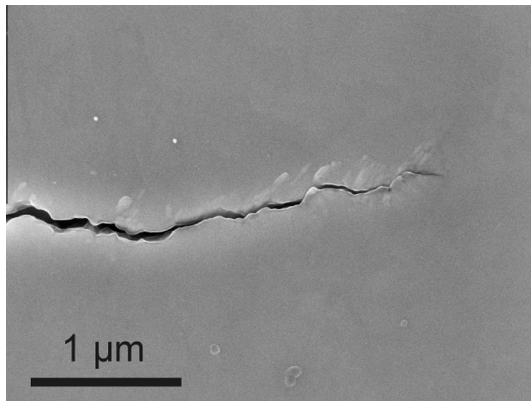


Fig. 3. Example of an open crack after compression–compression fatigue loading.

$$K_{\mathrm{J}} = \tau \sqrt{\pi a} Y_{\mathrm{J}}; \quad \mathrm{J} = \mathrm{II, III} \tag{1}$$

where $a = l_{\mathrm{n1}} + l_{\mathrm{o}} + l_{\mathrm{s}}/2$ is the total crack length.

An example of $K_{\mathrm{II}}$ and $K_{\mathrm{III}}$ dependences on the angle $\varphi$ is presented as the polar diagram in Fig. 5. Details of the
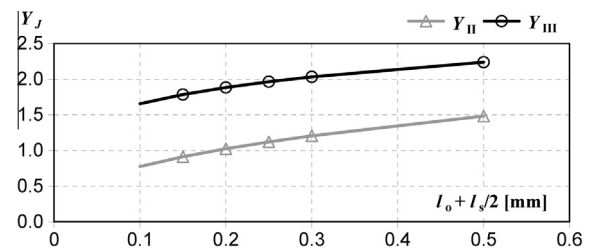


Fig. 4. Geometrical factors $Y_{\mathrm{II}}$, $Y_{\mathrm{III}}$ as functions of fatigue crack length $l_{\mathrm{o}} + l_{\mathrm{s}}/2$ for the notched cylindrical pure shear specimen.

FEM ANSYS model and the $K$-calibration procedure based on the $J$-integral are described elsewhere [15]. This approach, based on one sub-model, was refined by an additional second sub-model to obtain particularly precise $K$-values around the circumferential pre-crack.

Pure mode II experiments were performed on compact tension shear (CTS) specimens using the mode I + II device (Fig. 2). SIFS were calculated according to the formula

$$K_{\mathrm{II}} = \frac{P}{Wt} \sqrt{\pi a} \cdot Y_{\mathrm{II}} \tag{2}$$

where $P$ is the applied force, $W$ is the specimen width, $t$ is the specimen thickness, $a = l_{\mathrm{n2}} + l_{\mathrm{o}} + l_{\mathrm{s}}/2$ is the total crack length, $l_{\mathrm{n2}} = 21$ mm is the notch depth and $Y_{\mathrm{II}}$ is the geometrical factor [16].

Pure mode III experiments were also conducted by means of a special device transforming tensile or compressive force to torsion loading of cracked cylindrical specimens. The specimens were fixed into this device by ring clamping elements and loaded by cyclic torque $T$. SIFs were calculated according to an asymptotic relationship (3) published in Ref. [17]:

$$K_{\mathrm{III}} = \frac{16T}{\pi d^3} \cdot \sqrt{\pi a} \cdot Y_{\mathrm{III}} \tag{3}$$

where $a = l_{\mathrm{n1}} + l_{\mathrm{o}} + l_{\mathrm{s}}/2$ and
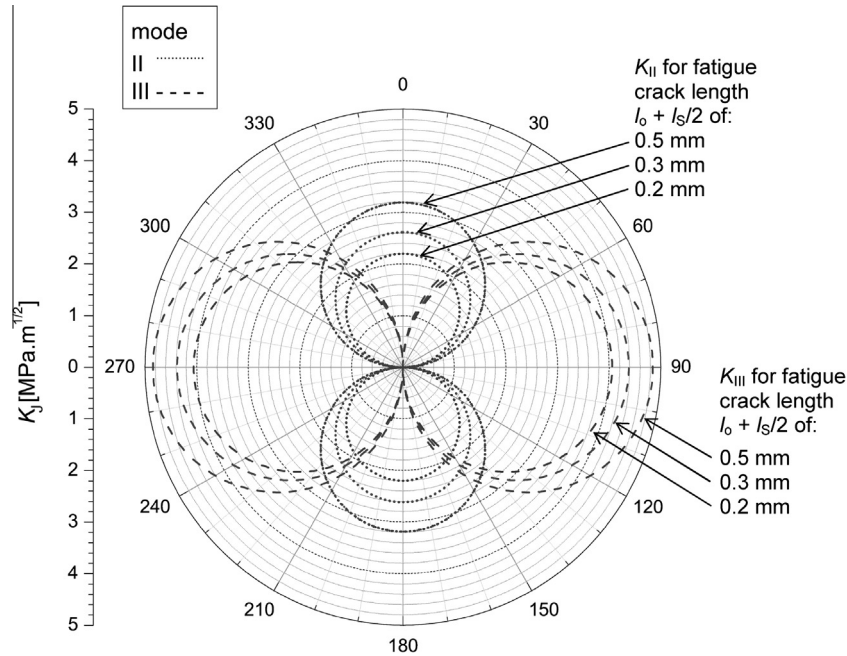
Fig. 5. Example of $K_{II}$ and $K_{III}$ dependences on the angle $\varphi$ for various fatigue crack lengths $l_o + l_s/2$ and the loading force of 7355 N for the notched cylindrical pure shear specimen.

$$Y_{III} = \frac{3}{8}\sqrt{\xi}\left(1 + \frac{1}{2}\xi + \frac{3}{8}\xi^2 + \frac{5}{16}\xi^3 \frac{35}{128}\xi^4 + 0.208\xi^5\right);$$

$$\xi = \frac{d}{D} \qquad\qquad (4)$$

## 3. Crack growth data

The crack growth rate data obtained under remote modes II and III are, for both investigated materials, plotted as diagrams $\Delta a/\Delta N$ vs. $\Delta K$ in Fig. 6, where $\Delta a = l_s$. The values $\Delta a/\Delta N$ were determined as averaged crack growth rates of the shear-mode cracks during $\Delta N$ cycles. In all experiments, the related ratio $\Delta a/a \approx 0.01$ was very small and the corresponding changes of $\Delta K$ during the shear-mode crack growth could be therefore considered to be negligible. These data were fit using the equation $\Delta a/\Delta N = A(\Delta K^n - \Delta K_{th}^n)$ suitable for the near- threshold region [18] despite $\Delta a/\Delta N$ being not a real crack propagation rate. Note that the data related to $\Delta a/\Delta N = 10^{-13}$ correspond to the absence of crack growth. In general, a rather high scatter of $\Delta a/\Delta N$ values was observed especially in the near-threshold region. The mode II data for pure shear and CTS specimens show a good agreement. The mode III data obtained for pure shear and torsion specimens are also in good agreement, although the torsion data in ferrite indicate slightly higher crack growth rates. This can be explained by the fact that, unlike in pure shear, the torsional mode III cracks can get some mode I support by a deflection to planes with non-zero normal stresses. Therefore, the topology profiles on the torsion fracture surfaces exhibit higher mean deflection angles than those on

the pure-shear specimens (see angles $\beta_{III}$ for ferrite in the next section).

The values of thresholds $\Delta K_{IIth}$ and $\Delta K_{IIIth}$ are shown in Table 1 as indicated by the fitting curves in Fig. 6. Due to the above-mentioned technique of specimen preparation, these values are very close to the effective ones. For both investigated materials, the values of $\Delta K_{IIIeff,th}$ are ~1.7 times higher than those of $\Delta K_{IIeff,th}$. This clearly reveals that the material fatigue resistance to crack growth in mode III is higher than that in mode II.

## 4. Quantitative fractography

The crack path and the surface topography were studied by means of stereophotogrammetry with the SEM [19,20]. A pair of fracture surface images was acquired by tilting the specimen by a small angle (5° or 10°). The software package MeX™ was used for three-dimensional (3-D) reconstruction of the fracture surfaces and measurements by means of the profile analysis to determine local deflection and twisting angles of the crack with respect to the remote shear direction. A more detailed description of the fracture morphology for modes II and III in ferrite and austenite is presented elsewhere [21].

The mean values and standard deviations of facet angles $\alpha_{II}$ and $\alpha_{III}$ parallel to the respective remote shear direction under modes II and III loading are presented in Table 2 for both materials. These angles indicate the levels of deflection and twisting of crack fronts relevant for mode I branching. The angles $\beta_{II}$ and $\beta_{III}$ perpendicular to the shear direction are also introduced in Table 2. In the special case of torsional loading, the deflection angles $\beta_{III}$ also reflect an
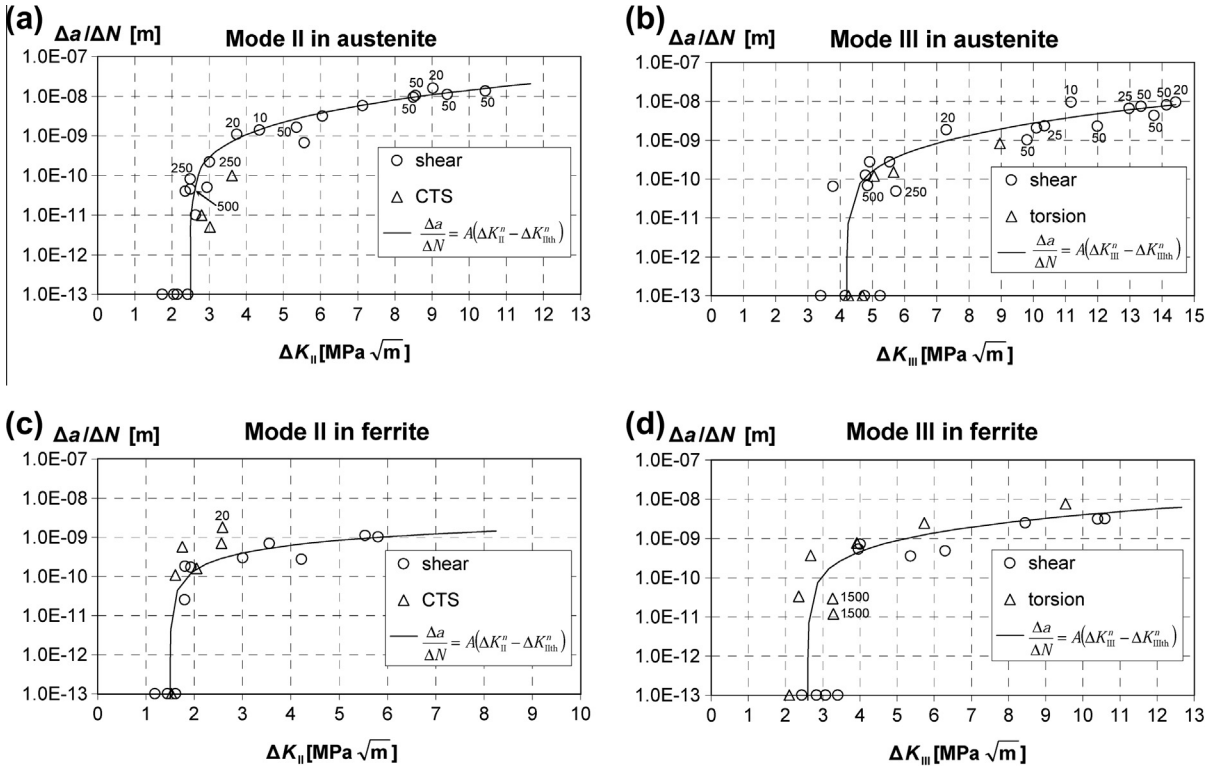
Fig. 6. Mean crack growth rate data for ferrite (ARMCO iron) and the austenitic steel obtained under remote modes II and III loading. The number of loading cycles is indicated in thousands of cycles ($\Delta N/1000$) near some data points. For the data where no number is indicated, the number of loading cycles was $\Delta N = 10^5$. It should be noted that the calculated $\Delta K_{II}$ and $\Delta K_{III}$ are global $K$ values which do not take into account crack branching. (a) ARMCO iron under mode II loading. Circles – pure shear specimens, triangles – CTS specimens. (b) Austenitic steel under mode II loading. Circles – pure shear specimens, triangles – CTS specimens. (c) ARMCO iron under mode III loading. Circles – pure shear specimens, triangles – torsion specimens, (d) austenitic steel under mode III loading. Circles – pure shear specimens, triangles – torsion specimens.

Table 1
Measured effective crack growth thresholds for ferrite and austenite.

| | | |
|---|---|---|
| $\Delta K_{IIeff,th}$ | Ferrite | 1.5 |
| (MPa m$^{1/2}$) | Austenite | 2.5 |
| $\Delta K_{IIIeff,th}$ | Ferrite | 2.6 |
| (MPa m$^{1/2}$) | Austenite | 4.2 |

amount of the local mode I support at the crack front. Indeed, the torsional mode III cracks can easily become mode-I controlled by deflections close to 45°.

In austenite, the deflection angles $\alpha_{II}$ measured on both the shear and CTS specimens are close to the theoretical value of 70.5° of mode I branches. On planes with these deflection angles the dislocation slip cannot be triggered since the Schmid factor is close to zero. This means that the elementary mode I branch could not be created by the dislocation emission on the plane of the branch. After that, the branched mode II cracks continued to propagate in the local opening mode. A steep step formed in this way on the fracture surface is depicted in Fig. 7 along with the

Table 2
Deflection and twisting angles (°) corresponding to the direction parallel ($\alpha_{II}$ and $\alpha_{III}$) and perpendicular ($\beta_{II}$ and $\beta_{III}$) to the remote shear vector.

| Mode | Angle | Branch type | Material | Specimen | |
|---|---|---|---|---|---|
| | | | | Shear | CTS/torsion |
| II | $\alpha_{II}$ | Deflection | Ferrite | $18 \pm 17$ | $19 \pm 8$ |
| | | | Austenite | $66 \pm 4$ | $68 \pm 9$ |
| | $\beta_{II}$ | Twisting | Ferrite | $18 \pm 16$ | $25 \pm 20$ |
| | | | Austenite | $7 \pm 5$ | $16 \pm 8$ |
| III | $\alpha_{III}$ | Twisting | Ferrite | $19 \pm 13$ | $13 \pm 10$ |
| | | | Austenite | $33 \pm 23$ | $45 \pm 8$ |
| | $\beta_{III}$ | Deflection | Ferrite | $18 \pm 13$ | $33 \pm 31$ |
| | | | Austenite | $19 \pm 14$ | $29 \pm 18$ |

related crack-path profile. Both the fracture morphology and the profile of the step are smooth, without any sign of crystallographic facets, which can also be seen in Fig. 8 in more detail. This means that the growth of the mode I branch is controlled by a simple rule, i.e. the maximum-tensile-stress criterion. The twisting angles $\alpha_{III}$ on fracture surfaces of shear and torsion specimens also approach the theoretical value of $45°$ for a mode I branch under the remote mode III loading. Consequently, the Schmid factor on the related planes is nearly zero and the elementary mode I branches (followed by the factory-roof-like crack propagation) are not formed by dislocation emission. The factory-roof morphology was created in both shear and torsion specimens as depicted in Figs. 9 and 10 along with the related crack-front profiles. This reveals that such a type of morphology can be formed not only under torsion but also under simple shear. Thus, all the remote shear-mode cracks in austenite propagated locally under nearly pure opening modes.

On the other hand, the mean values of angles $\alpha_{II}$ and $\alpha_{III}$ for ferrite are rather small. Examples of the related fracture morphology are shown in Figs. 11 and 12. This indicates the local crack growth under dominant shear modes with a relatively small support of mode I. It should be noted that the mean deflection angle $\beta_{III}$ measured from the fracture surfaces of torsional specimens is rather high. This means that the torsional cracks propagated under a high mode-I support which was already reported in Ref. [22] for specimens made of high strength steel. In Fig. 12 related to the remote mode III, the fringe patterns that highlight

the positions of local crack front elements inside individual facets are mostly not with respect to the applied shear direction. The arrows indicate the local crack propagation directions which mostly possess a high mode II component parallel with the direction of applied shear stress. This corresponds to the model of local mode-II controlled micromechanism of the remote mode III crack propagation [22], including some support of opening mode. Both mode II and mode III fracture surfaces suggest an influence of crystallography on the crack growth in ferrite, which can be also clearly seen in the fracture profile in Fig. 12. No traces of abrasive wear were found on fracture surfaces of specimens near the threshold. Thus, the cracks in ferrite locally propagated in crystallography assisted mixed mode I + II + III with negligible interaction of crack-wake asperities.

## 5. Discussion

In Tables 1 and 2 the main experimental results are summarized. Ferrite and the austenitic steel exhibit a significantly different behavior in two aspects: the crack path and the absolute values of the effective threshold values. The ferrite has a significantly smaller $\Delta K_{IIeff,th}$ and $\Delta K_{IIIeff,th}$ than the austenite. In the austenite, the mode II cracks immediately create a mode I branch and the mode III cracks instantly start to develop a factory-roof-like crack shape. The two most physical based explanations for the occurrence of the threshold of stress intensity range differ with respect to the generation of the new fracture surface [23–27]. In both models, the threshold is a consequence of the discrete nature of plasticity, i.e. the explanations are dislocation based. In the following, these two models will be briefly introduced and analyzed whether they can elucidate the observed shape of the crack path or not. The relation between the $\Delta K_{eff,th}$ values of mode I, mode II and mode III and the difference between these values in austenite and ferrite will be discussed afterwards.

In the first model [23,25] the fatigue crack propagation is a consequence of a deformation-induced generation of new surface in terms of the formation of dislocation slip steps on a free surface. The crack propagates by the creation of new fracture surface by blunting during loading and re-sharpening during unloading, as schematically depicted in Fig. 13. The mechanism is similar to the models proposed by Pelloux [28] or Neumann [29] or the models based on the direct observation of the crack propagation at larger crack propagation rates [30,31]. Due to both the small cyclic plastic zone near the threshold and the limited number of available dislocation sources, the emission of dislocations from the crack tip will dominate the cyclic plastic deformation. Such generated dislocations will then automatically blunt the crack. During unloading, the dislocation will return to the crack tip and re-sharpen it. The newly created surface will not re-weld due to oxidation. As a consequence, the crack will propagate cycle per cycle with a growth rate proportional to the cyclic crack tip
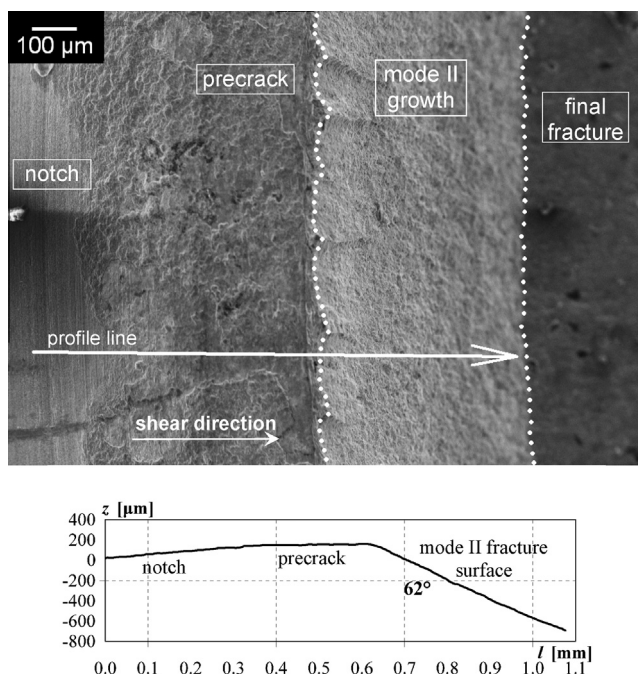


Fig. 7. Fracture morphology and profile of a remote mode II crack in austenite. The mode II region represents a mode I step (branch) deflected by $62°$ of the maximum shear plane as clearly visible on the associated part of the profile ($\Delta K_{II} = 9.3$ MPa m$^{1/2}$, $N = 5 \times 10^4$).
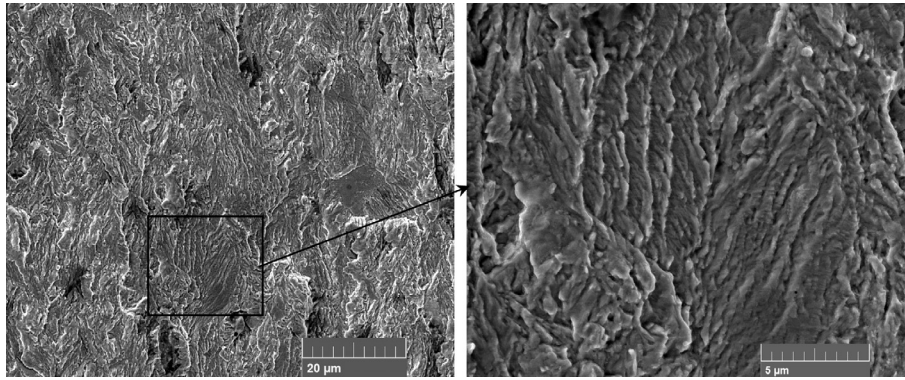
Fig. 8. Non-crystallographic morphology of the mode I step in Fig. 7 in more detail.
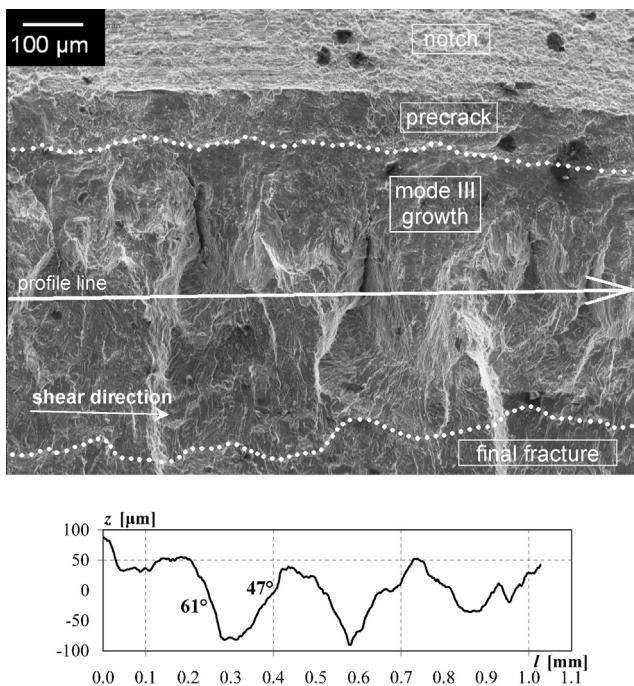


Fig. 9. Mode III fracture morphology of an austenite specimen loaded in the remote simple shear. Due to the factory-roof profile the local crack-tip loading is in mode I ($\Delta K_{III} = 13.4$ MPa m$^{1/2}$, $N = 5 \times 10^4$).



Fig. 10. Mode III fracture morphology and factory-roof profile in austenite specimen loaded in torsion ($\Delta K_{III} = 9.0$ MPa m$^{1/2}$, $N = 10^5$).

opening displacement. Since a certain stress concentration, i.e. a certain local stress intensity, is needed to emit a dislocation from the crack tip and due to the fact that the dislocations move away from this stress concentration, a certain minimum $\Delta K$ is necessary to cause cyclic plastic deformation: this $\Delta K$ determines $\Delta K_{eff,th}$. For a symmetric arrangement of slip planes the crack propagates in an ideal mode I manner, even on the local scale. For an asymmetric arrangement of slip planes, the usual case, the crack should propagate predominately along the dominant slip plane, i.e. in a crystallographic manner.

The second model, proposed by Deshpande et al. [26,27], assumes that plasticity is caused by internal dislocation sources only. The generated dislocations form the plastic zone, with some of the dislocations running out at the crack flanks. Most of the dislocations shield the crack tip from the external loading, which allows applying stress intensity factors larger than the Griffiths stress intensity $K_G$.

However, a few dislocations also cause anti-shielding. If one of them comes very close to the crack tip it can induce a decohesion. In other words, when the tensile stress field in front of the crack and that of the dislocation have a sufficient overlap, the crack will propagate by decohesion until it reaches the anti-shielding dislocation, as schematically depicted in Fig. 13.

In our opinion this process can only occur if the anti-shielding dislocation is just a few lattice spacings away from the crack front. The crack should not propagate on a slip plane; rather it would predominately grow under
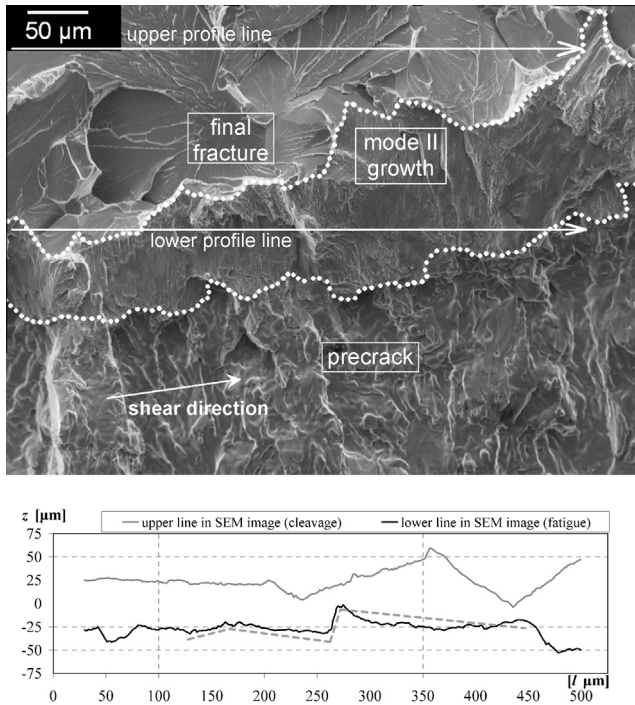
Fig. 11. Mode II fracture morphology along with fatigue and cleavage profiles in the ferrite specimen loaded in the simple shear. The plotted dashed line corresponds to the fatigue facets visible on the SEM picture in the mode II growth region. The upper line indicates comparably sized cleavage facets in the final fracture region related to individual grains ($\Delta K_{II} = 3.6$ MPa m$^{1/2}$, $N = 10^5$).
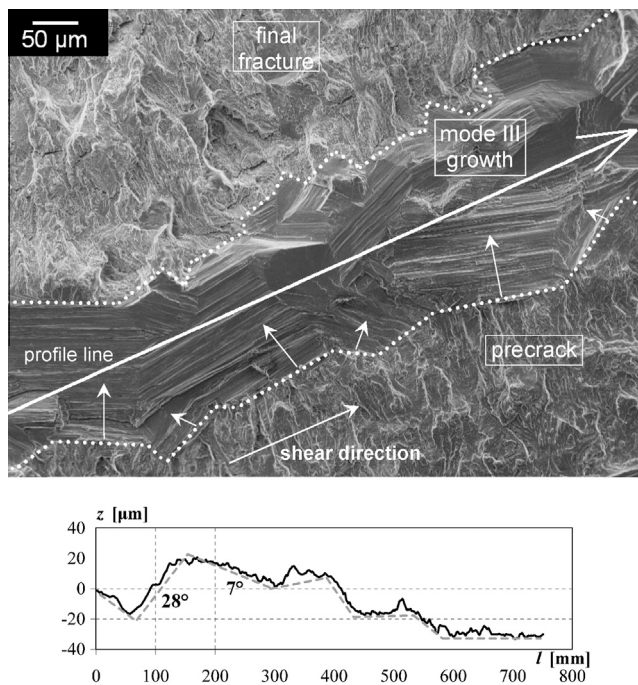


Fig. 12. Mode III fracture morphology and profile in the ferrite specimen loaded in torsion. The plotted dashed line corresponds to facets in the mode III region marked in the SEM image ($\Delta K_{III} = 3.3$ MPa m$^{1/2}$, $N = 1.5 \times 10^6$).

the local mode I on a cleavage plane or in a non-crystallographic manner.

Both models give mode I threshold values somewhat smaller than the experimentally observed values, which might be a consequence of the 3-D nature of the crack. Both mechanisms are reasonable and, in principle, they might be responsible for the threshold at different positions along the crack front in a material. The mechanism which delivers the smallest local $\Delta K_{eff,th}$ should determine whether the crack can locally propagate or not.

Let us now discuss in which direction a crack should propagate under the mode II loading according to the two different crack propagation models. In the deformation model, the dislocations generated at the crack tip will cause crack sliding displacements and generate new surfaces, see Fig. 13. Therefore, the crack should preferentially propagate in a mode II manner, with small inclinations to the direction where the tensile stresses are developed during the crack-tip loading. Such a small deflection generates an opening of the crack during loading, thus avoiding crack closure and friction of the crack flanks.

For the mode III case the explanation is more difficult. In the ideal deformation-based model [25], the slip plane of screw dislocations is co-planar with the crack plane and their Burgers vector is parallel to the crack front. If mode III cyclic plastic shear displacements appear at that front then no new fracture surface is generated and the crack does not propagate at all. This corresponds to the phenomenon that a deformation produced by dislocations with a Burgers vector parallel to a free surface does not cause surface steps. However, such an ideal crack/slip configuration is very unlikely. The Burgers vector will always have a certain component in the crack propagation direction. Hence, even in the case of an ideal straight crack front the mode III loading will initiate not only a plastic mode III crack tip displacement but also generate a certain sliding displacement in the mode II direction, generating new surfaces.

A deviation from the ideal straight crack front is a further reason why a mode III crack can propagate by deformation-induced new surface generation. A deviation in the plane of the crack locally generates a mixture between mode II and mode III loading. Even if the local mode III segments of the crack front do not propagate, the mode II segments should propagate. In the pure deformation-based model, the crack will propagate in the plane of the crack.

When considering the decohesion model, the probability of having a slip plane parallel to the crack plane and internal dislocation sources co-planar with the crack plane is very low. Therefore, the generated dislocations will not cause a plastic crack tip sliding displacement. One part of the generated dislocations will move in front of the crack tip, the other will move to the crack tip and behind, depending on the location of the dislocation source. A few dislocations moving behind the crack tip will enter the crack flank; the others will move behind the crack tip. Some of these dislocations will come very near to the crack tip. These dislocations can generate a local decohe-
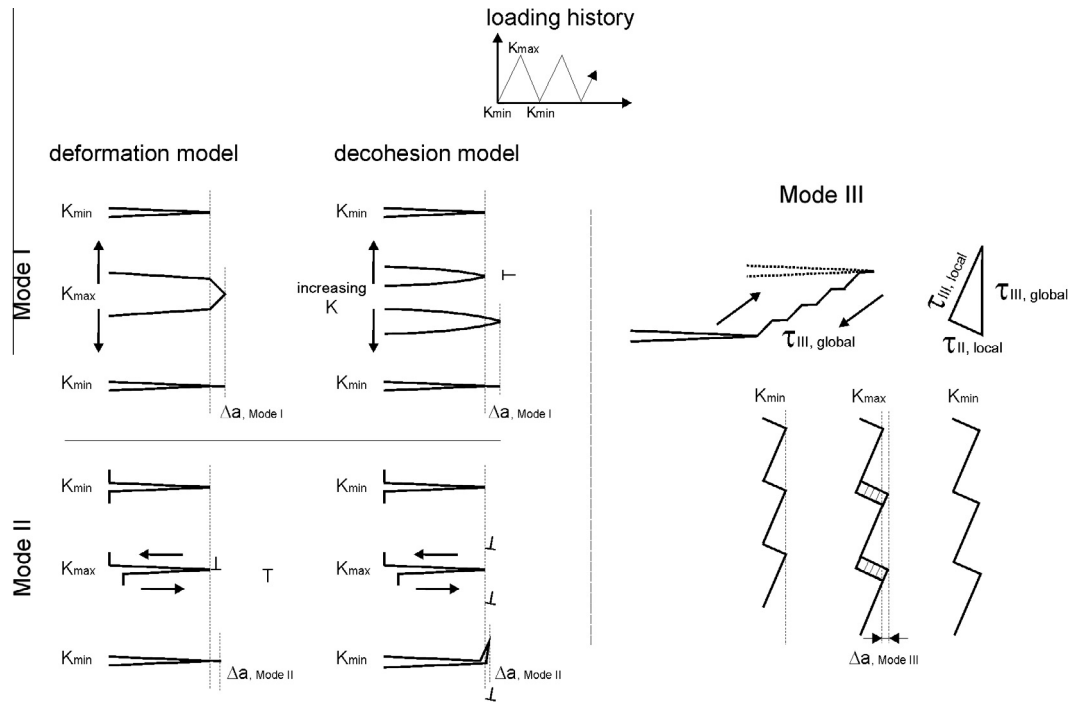
Fig. 13. Comparison of the proposed different types of fatigue crack propagation mechanisms near the threshold. Illustration of the deformation and decohesion model for the different loading modes.

sion due to a superposition of their tensile stress field and the tensile stress field of the crack. The most probable crack propagation direction is determined by a maximum tensile component of the crack tip stress field, i.e. by the maximum of local $k_I$ (see Fig. 13).

For the ideal mode III crack with plane crack flanks and straight crack front, the explanation of crack growth by decohesion is not as straightforward, because such cracks do not generate a tensile stress singularity. Only the tensile stresses generated from the edge segments of the dislocations near the crack flanks can cause decohesion. However, even in the case of decohesion fatigue crack propagation mechanism, the crack front segments locally loaded in mode II will propagate in the same manner as under the pure global mode II loading. This means that the local mode II segments of the mode III crack front will deflect from the macrocrack plane similarly to the mode II crack.

In summary, a mode II and a mode III crack in the case of the deformation-induced surface generation should preferentially propagate in the plane of the pre-crack, whereas in the case of the dislocation induced or dislocation supported de-cohesion, the crack should deflect. The mode II crack should globally tilt and the mode III should locally twist. A comparison of the characteristic fractographic features near the threshold of stress intensity range indicates that the crack in ferrite propagates by the deformation model. On the other hand, it seems that dislocation-stimulated decohesion dominates the onset of fatigue crack propagation in the austenitic steel near the threshold, i.e. the creation of mode I branches – see Figs. 7 and 9.

Although both decohesion and emission mechanisms might, in principle, be involved during the further growth of mode I crack branch, we believe that decohesion mechanism remains the controlling one. This conclusion is supported by the fact that such a difference can also be observed in the case of the remote mode I near-threshold crack growth in ferrite and austenite, as illustrated in Fig. 14. In ferrite, a crystallographic propagation along slip planes can be clearly identified. In austenite a non-crystallographic morphology of the fracture surface similar to that for mode I branch in Fig. 8 can be seen.

The experimentally determined differences in the effective thresholds can be compared with predictions based on the assumed crack growth models explaining the fractographic features. In the case of the deformation-induced surface generation the ratio between $\Delta K_{\mathrm{Ieff,th}}$ and $\Delta K_{\mathrm{IIeff,th}}$ should be equal to the ratio of the local stress intensities $k_{\mathrm{Ie}}$ and $k_{\mathrm{IIe}}$ to generate an edge dislocation under modes I and II, respectively, i.e.

$$\frac{\Delta K_{\mathrm{Ieff,th}}}{\Delta K_{\mathrm{IIeff,th}}} = \frac{k_{\mathrm{Ie}}}{k_{\mathrm{IIe}}} \tag{6}$$

There are several estimations of $k_{\mathrm{Ie}}$ and $k_{\mathrm{IIe}}$ in the literature [25]; the differences are relatively small. The ratio of $k_{\mathrm{Ie}}/k_{\mathrm{IIe}}$ is ~2, which fits well with measured ratios of $\Delta K_{\mathrm{Ieff,th}}/\Delta K_{\mathrm{IIeff,th}}$ for ferrite. The $k_{\mathrm{IIIe}}$ values for the emission of screw dislocations at the mode III crack front (see, for example, Ref. [32]) are estimated to be somewhat smaller than those for $k_{\mathrm{IIe}}$, which would not fit the ratio of measured threshold values. However, if one supposes that
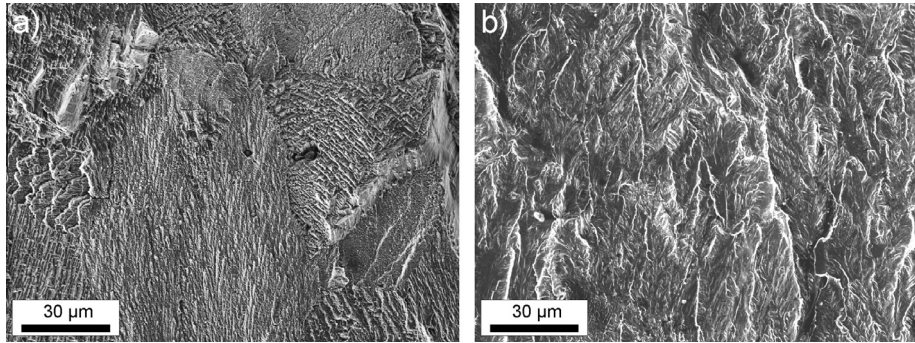
Fig. 14. Comparison of the typical fatigue fracture surface in mode I in the near-threshold regime: (a) ferrite and (b) the austenitic steel. In the case of the austenitic steel the crack propagates without exhibiting crystallographic features whereas in ferrite, a tendency of crack propagation along crystallographic planes is visible.

only the local mode II segments propagate under global mode III loading then the local mode II stress component should only be taken into account. Assuming that the mean deviation angle from the straight crack front is 30°, the ratio of the local mode II and mode III shear stress is $\tau_{II}/\tau_{III} = 0.5$, which follows from a geometrical separation of the local shear stresses. Therefore, the ratio $\Delta K_{IIIeff,th}/\Delta K_{IIeff,th}$ should be ~2, which is in good agreement with the measured values for ferrite.

If the decohesion controls the fatigue crack propagation both the tensile stress field of the crack and the tensile stress field of a dislocation for the different loading cases should control the effective threshold. The near crack tip tensile stress is determined by the local $k_I$. The maximum of the local $k_I$ for a global $K_{II}$ is obtained for a kink angle $\psi$ of $-70°$ [33,34]:

$$k_1 = -\frac{3}{4}\left(\sin\frac{\psi}{2} + \sin\frac{3\psi}{2}\right)K_{II} = 1.15K_{II} \qquad (7)$$

The local $k_I$ under global mode I loading has a maximum for the straight crack where $k_I = K_I$. If one assumes that the probability to move dislocation with its tension stress field close to the crack tip is the same for the mode I and the kinked mode II, then

$$\Delta K_{IIeff,th} = \frac{\Delta K_{Ieff,th}}{1.15} \qquad (8)$$

which should result in a $\Delta K_{IIeff,th}$ of ~2 MPa m$^{1/2}$. However, the measured $\Delta K_{IIeff,th}$ value is ~2.5 MPa m$^{1/2}$. This small discrepancy might be caused by the different probability to move antishielding dislocations sufficiently close to the crack tip in the case of a global mode I and mode II crack. An ideal mode III crack has no tensile stress component; however, a deviation from the ideal straight crack front can generate local mode II and local mode I components. Assuming a similar geometrical deviation as that for the estimation of the ratio $\Delta K_{IIIeff,th}/\Delta K_{IIeff,th}$ in the deformation model and the decohesion running only near the local mode II segments, the ratio $\Delta K_{IIIeff,th}/\Delta K_{IIeff,th}$ should

be similar for both the austenite and the ferrite. This is well fulfilled.

The fact that the crack growth near the threshold in austenite and ferrite is controlled by different mechanisms (decohesion or deformation) might be attributed to the number of slip systems available for shear crack propagation in these metals. In the bcc structure of ferrite, a dense spatial set of possible slip systems $\langle 111\rangle\{110\}$ and $\langle 111\rangle\{112\}$ is available for dislocation emission and slip. This set consists of slip planes mutually exhibiting as much as nine different angles in the range of 0–90° [35]. Therefore, there is a high probability of finding slip planes in grains, adjacent to the pre-crack front, which exhibit the Schmid factor comparable to that of the pre-crack plane with maximum shear stress. Consequently, the crack can easily propagate along slip planes according to the deformation-based model by only slight deviations or twists with respect to the pre-crack plane in ferrite (low averaged deflection and twist angles in Table 2). On the other hand, the possible slip systems $\langle 110\rangle\{111\}$ in the fcc structure of austenite form a very thin set of planes exhibiting only one angle between 0° and 90°. In austenite, the crystallographically controlled crack growth becomes improbable. This hypothesis must be verified by additional experiments on different fcc and bcc materials.

At the end it should be noted that the two models used to explain the differences between austenite and ferrite are not as diverse as they look. Both models originally used a two-dimensional dislocation description of deformation and propagation of a cyclically loaded crack which, in some cases, represents a good approximation [25]. In many cases, however, the 3-D nature of dislocation slip may become important and bring the two models closer together, for example the emission of dislocations on an inclined and twisted plane. Indeed, even such emitted dislocations cause blunting and can produce anti-shielding dislocations, which may trigger the decohesion process.

## 6. Summary

The near-threshold behavior of mode II and mode III long fatigue cracks in the ferritic and the austenitic steel were experimentally studied using various sample geometries. In this way, the effective threshold values $\Delta K_{\mathrm{IIeff,th}}$ and $\Delta K_{\mathrm{IIIeff,th}}$ could be obtained. 3-D topological data obtained by examination of fracture surfaces were utilized to identify crack growth micromechanisms in both materials. The main results of this study can be summarized as follows:

(i) Effective thresholds of stress intensity range for ferrite $\Delta K_{\mathrm{IIeff,th}} = 1.5$ MPa m$^{1/2}$ and $\Delta K_{\mathrm{IIIeff,th}} = 2.6$ MPa m$^{1/2}$ were lower than those for austenite $\Delta K_{\mathrm{IIeff,th}} = 2.5$ MPa m$^{1/2}$ and $\Delta K_{\mathrm{IIIeff,th}} = 4.2$ MPa m$^{1/2}$.

(ii) In both investigated materials, the effective thresholds for mode III were $\sim$1.7 times higher than those for mode II.

(iii) In austenite, mode I branching of both the mode II and mode III cracks started at the very onset of crack growth. This was not the case in ferrite where all cracks propagated predominantly in a shear mode with a small mode I contribution. Here, the crack path seemed to be crystallographically assisted.

These experimental results can be understood in terms of crack growth micromechanisms according to the deformation model in ferrite and the decohesion model in austenite. The dissimilarity in the crack-growth mechanisms in ferrite and austenite may be caused by the difference in the number of available slip systems in bcc and fcc metals.

## Acknowledgements

## References

[1] Ritchie RO. Mater Sci Eng A 1988;103:15–28.

[2] Suresh S. Fatigue of materials. Cambridge: Cambridge University Press; 1998.

[3] Tschegg EK. Acta Metall 1983;31:1323–30.

[4] Pokluda J, Šandera P. Micromechanisms of fracture and fatigue. London: Springer; 2010.

[5] Murakami Y. Metal fatigue: effects of small defects and nonmetallic inclusions. Oxford: Elsevier; 2002.

[6] Pinna C, Doquet V. Fatigue Fract Eng Mater Struct 1999;22:173–83.

[7] Pokluda J, Trattnig G, Martinschitz C, Pippan R. Int J Fatigue 2008;30:1498–506.

[8] Pokluda J, Slámečka K, Šandera P. Eng Fract Mech 2010;77:1763–71.

[9] Pook LP. Crack paths. Southampton: Wit Press; 2002.

[10] Doquet V, Bertolino G. Eng Fract Mech 2008;75:3399–412.

[11] Pippan R, Berger M, Stüwe HP. Metall Trans 1987;18A:429–35.

[12] Pippan R. Eng Mater Struct 1987;9:319–28.

[13] Pippan R. Mater Sci Eng A 1991;138:1–14.

[14] Zhao J, Guo W. Eng Fract Mech 2012;92:72–88.

[15] Horníková J, Šandera P, Pokluda J. Key Eng Mater 2011;452–453:673–6.

[16] Richard HA, Benitz K. Int J Fracture 1983;22:R55–8.

[17] Benthem JP, Koiter WT. In: Sih GC, editor. Mechanics of fracture: method of analysis and solutions of crack problems. Leyden: Noordhof International; 1973.

[18] Klesnil M, Lukáš P. Fatigue of metallic materials. Amsterdam: Elsevier; 1992.

[19] Stampfl J, Scherer S, Gruber M, Kolednik O. Appl Phys A 1996;63:341–6.

[20] Semprimoschnig COA, Stampfl J, Pippan R, Kolednik O. Fatigue Fract Eng Mater Struct 1997;20:1541–50.

[21] Vojtek T, Pokluda J. In: Carpinteri A, Iacoviello F, Pook LP, Susmel L, editors. Proceedings of Crack Paths (CP 2012). Gaeta: Gruppo Italiano Frattura; 2012. 727–34.

[22] Pokluda J, Pippan R. Fatigue Fract Eng Mater Struct 2005;28:179–86.

[23] Pippan R. Acta Metall Mater 1991;39:255–62.

[24] Pippan R, Weinhandl H. Int J Fatigue 2010;32:1503–10.

[25] Riemelmoser FO, Gumbsch P, Pippan R. Mater Trans 2001;42:2–13.

[26] Deshpande VS, Needleman A, Van der Giessen E. Acta Mater 2001;49:3189–203.

[27] Van der Giessen E, Deshpande VS, Cleveringa HHM, Needleman A. J Mech Phys Solids 2001;49:2133–53.

[28] Pelloux RMN. Eng Fract Mech 1970;7:235–47.

[29] Neumann P. Acta Metall 1974;22:1155–65.

[30] Vehoff H. Acta Mater 1980;28:265–72.

[31] Pippan R, Zelger C, Gach E, Bichler C, Weinhandl H. Fatigue Fract Eng Mater Struct 2011;34:1–16.

[32] Ohr SH. Mater Sci Eng 1985;72:1–35.

[33] Bilby BA, Cardew GE, Howard IC. In: Taplin DMR, editor. Fracture 1977, vol. 3. New York: Pergamon Press; 1977.

[34] Cotterell B, Rice J. Int J Fracture 1980;16:155–69.

[35] Parker CB. Encyclopaedia of physics. 2nd ed. New York: McGraw Hill; 1994.